

Complex magnetic ordering as a driving mechanism of multifunctional properties of Heusler alloys from first principles[★]

Peter Entel^{1,a}, Mario Siewert¹, Markus E. Gruner¹, Heike C. Herper¹, Denis Comtesse¹, Raymundo Arróyave², Navedeep Singh², Anjana Talapatra², Vladimir V. Sokolovskiy^{3,4}, Vasiliy D. Buchelnikov⁴, Franca Albertini⁵, Lara Righi⁶, and Volodymyr A. Chernenko^{7,8}

¹ Faculty of Physics and CENIDE, University of Duisburg-Essen, 47048 Duisburg, Germany

² Department of Mechanical Engineering, Texas A&M University, College Station, 77843 Texas, USA

³ National University of Science and Technology 'MISIS', 119049 Moscow, Russia

⁴ Condensed Matter Physics Department, Chelyabinsk State University, 454001 Chelyabinsk, Russia

⁵ IMEM Department of Magnetic Materials, CNR, Parco delle Scienze 37/a, 43010 Parma, Italy

⁶ Dipartimento Chimica GIAF, Università di Parma, 43124 Parma, Italy

⁷ Universidad del País Vasco, Departamento de Electricidad y Electrónica, P.O. Box 644, 48080 Bilbao, Spain

⁸ Ikerbasque, Basque Foundation for Science, 48011 Bilbao, Spain

Received 12 October 2012 / Received in final form 12 December 2012

Published online 20 February 2013 – © EDP Sciences, Società Italiana di Fisica, Springer-Verlag 2013

Abstract. First-principles calculations are used to study the structural, electronic and magnetic properties of (Pd, Pt)-Mn-Ni-(Ga, In, Sn, Sb) alloys, which display multifunctional properties like the magnetic shape-memory, magnetocaloric and exchange bias effect. The *ab initio* calculations give a basic understanding of the underlying physics which is associated with the complex magnetic behavior arising from competing ferro- and antiferromagnetic interactions with increasing number of Mn excess atoms in the unit cell. This information allows to optimize, for example, the magnetocaloric effect by using the strong influence of compositional changes on the magnetic interactions. Thermodynamic properties can be calculated by using the *ab initio* magnetic exchange parameters in finite-temperature Monte Carlo simulations. We present guidelines of how to improve the functional properties. For Pt-Ni-Mn-Ga alloys, a shape memory effect with 14% strain can be achieved in an external magnetic field.

1 Introduction

The magnetic Heusler alloys have become increasingly important because of their multifunctional properties which render them useful in different domains from spintronics to magnetic shape-memory and magnetocaloric technologies [1–11].

The strong magnetoelastic interactions in the magnetic Heusler alloys are responsible for novel functional properties such as the magnetic-shape memory and magnetocaloric effects (MSME & MCE). Both effects have recently been highlighted in references [1,4,5]. Another functional property is the exchange bias effect (EBE) [12–14], which has not yet been explored for practical applications. A necessary prerequisite for the materials to exhibit

the different smart features is the existence of martensitic transformations in the magnetic phase, the development of a large enough magnetocrystalline anisotropy and a very high mobility of the martensitic twin structures when a magnetic field or mechanical stress is applied. This is important for the MSME [15]. For the MCE we need, in addition, large isothermal entropy and adiabatic temperature changes which can be achieved if the first-order martensitic phase transition is merged with an abrupt change of magnetic order or the first-order magnetic phase transition itself [16]. Both types of transitions are called magnetostructural phase transitions which have been observed, e.g., for $\text{Ni}_{2+x}\text{Mn}_{1-x}\text{Ga}$ in the region $0.18 < x < 0.28$ [17].

An abrupt change of the magnetization with temperature has also been observed for a series of Heusler alloys of type $\text{Ni}_2\text{Mn}_{1+x}\text{Z}_{1-x}$ ($\text{Z} = \text{Ga, In, Sn, Sb}$) below the martensitic transformation from cubic austenite to martensite with tetragonality smaller than one ($c/a < 1$). This includes all modulated phases such as 10M and 14M

[★] Contribution to the Topical Issue “New Trends in Magnetism and Magnetic Materials”, edited by Francesca Casoli, Massimo Solzi and Paola Tiberto.

^a e-mail: entel@thp.uni-duisburg.de

as well because these structures can be described by the associated tetragonality due to the tiny monoclinic angle and weak modulation of the atomic positions. Alloys of this series exhibit competing ferromagnetic and antiferromagnetic exchange interactions. The antiferromagnetic features can be traced back to the observation that excess Mn in $\text{Ni}_2\text{Mn}_{1+x}\text{Z}_{1-x}$ mainly goes to the Z sublattice with a shorter distance to the surrounding Mn on the original Mn sublattice, which results in antiferromagnetic Mn-Mn configurations [6].

The appearance of antiferromagnetic exchange interactions has long ago been discussed for Ni-Mn-Sn alloys [18]. Recent small angle neutron scattering (SANS) studies on $\text{Ni}_{50-x}\text{Co}_x\text{Mn}_{40}\text{Sn}_{10}$ confirm complex changes of the magnetic behavior across the martensitic transformation [14]. This is a very important issue because the characteristic changes of martensitic and magnetic phase transitions with increasing x , i.e. with increasing valence electron concentration per atom (e/a), determine the phase diagrams as well as the multifunctional features near the martensitic phase transformation. Its understanding helps to design new materials by using quantum mechanical first-principles calculations. A state-of-the-art report of these efforts is the focus of this paper.

2 The MSME and its relation to martensitic transformations

The discussion of the MCE and its relation to the MSME in ferromagnetic Heusler alloys [4] shows the development in this field since the pioneering work by Ullakko et al. [19]. The magnetic field-induced (MFI) strain in a 14M $\text{Ni}_{48.8}\text{Mn}_{29.7}\text{Ga}_{21.5}$ sample has meanwhile reached 10% at 300 K in a magnetic field of less than 1 T [20] and a breakthrough in device development may be expected if one could still raise the martensitic transformation temperature M_S and Curie temperature T_C and simultaneously change the high brittleness of the samples to more ductile behavior.

This problem has not been solved yet and development of improved magnetic shape-memory alloys (MSMA) is needed. For instance, for a single variant $\text{Co}_{47.5}\text{Ni}_{22.5}\text{Ga}_{30.0}$ a large 7.6% MFI strain was observed in the martensitic phase at 300 K under a static compressive stress of about 12 MPa [21]. Another recent example of how to achieve a new MSMA is related to the partial substitution of Pt and Pd for Ni in Ni-Mn-Ga, which leads to monoclinic distortion involving the formation of a modulated 14M structure as in Ni_2MnGa , which allows for maximum strain effect of nearly 14% as estimated from the associated c/a tetragonality [22] (the $c/a < 1$ ratio as approximate of the modulated structure allows an estimate of the maximum strain achievable [23]). Our purpose is to use the predictive power of first-principles calculations to compare (Pt, Ni)-Mn-Z with the Ni-Mn-Z (Z = Ga, In, Sn, Sb) alloy series in order to check the suitability of (Pt, Ni)-Mn-Z for devices exploiting the MSME. Pt-Ni-Mn-Z alloys with Z = Ga were investigated experimentally

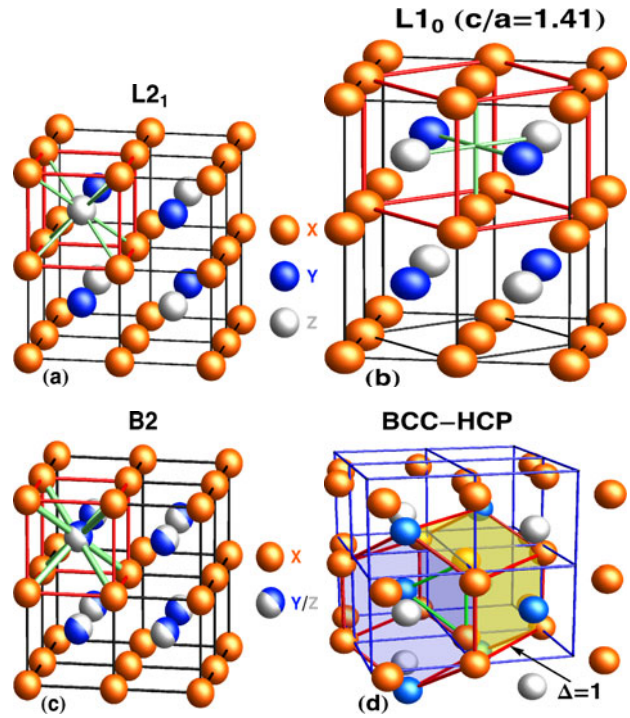


Fig. 1. (Color online) (a) The cubic $L2_1$ Heusler structure of X_2YZ with highlighted bcc-like arrangement of the atoms and (b) the tetragonal structure with $c/a = \sqrt{2}$ and highlighted fcc-like arrangement of the atoms. For the NiMn-based alloys, X stands for Ni, Y for Mn and Z for Ga, In, Sn or Sb. The tetragonal structure for $c/a < 1$ ($c/a = 0.83$) can undergo a shuffling transformation leading to the hcp structure. This shuffling can be described in the original bcc-like Heusler lattice by a shear mode motion of (011) successive planes in opposite directions in the original bcc-like Heusler lattice by $\pm a_0/12 [01\bar{1}]$. The complete bcc \rightarrow hcp transformation of the Heusler structure is displayed in panel (d). The high temperature B2-phase with disorder in the Y- and Z-sublattices is shown in panel (c).

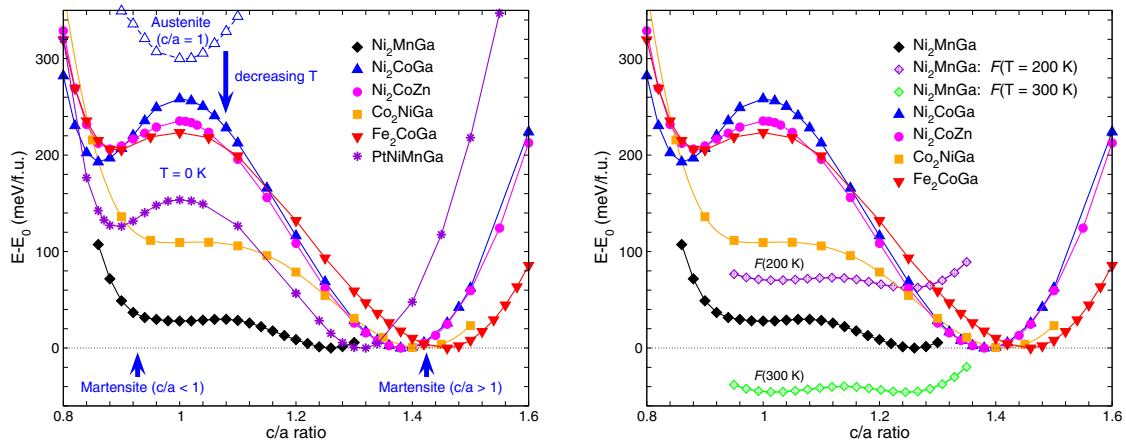
before [24,25] while preliminary results of first-principles calculations were reported in reference [22].

In what follows we discuss the interplay of structure and magnetism in order to understand the functional properties of the pseudobinary alloy series (Ni, Co)-Mn-(Ga, In, Sn, Sb) for which the stoichiometric formula unit is X_2YZ (conventional Heusler structure) or (XY)XZ (inverse Heusler structure [26]) and where each of the four interpenetrating fcc lattices is fully occupied (other structures like zinc-blende (CrSb) or half-Heusler alloys such as NiMnSb are not discussed, here we refer to the literature [2,7,8]). The cubic $L2_1$ structure of X_2YZ , as well as the tetragonally (Bain path [27,28]) and hexagonally (Burgers path [29,30]) distorted structures and the high-temperature B2 phase are shown in Figures 1a–1d. A selection of elements forming the constituents is given in Table 1 [31].

Figure 2 shows results of zero-temperature calculations of the total energy as a function of the tetragonal deviation from the cubic high-temperature austenitic $L2_1$ structure

Table 1. Preferred sites of different atoms in known Heusler alloys X_2YZ (X and Y are transition metals and Z is from the group of *sp* elements) [31].

Heusler alloy compositions												
Y sites					X sites					Z sites		
IIIB	IVB	VB	VIB	VIIB	VIIIIB	IB	IIB	IIIA	IVA	VA	VIA	
1												
2										B	C	N
3										Al	Si	P
4	Sc	Ti	V	Cr	Mn	Fe	Co	Ni	Cu	Zn	Ga	Ge
5	Y	Zr	Nb	Mo	Tc	Ru	Rh	Pd	Ag	Cd	In	Sn
6	La	Hf	Ta	W	Re	Os	Ir	Pt	Au	Hg	Tl	Pb
												Bi
												Po

**Fig. 2.** (Color online) Left: variation of the total energy at $T = 0$ K with tetragonality of different ferromagnetic Heusler systems showing the formation of two energy minima at $c/a < 1$ and at $c/a > 1$. In each case, the minimum of lowest energy is taken as energy zero [32,33]. The arrow indicates the change of the energy landscape from high-temperature austenite to low-temperature martensite. Right: for Ni_2MnGa , the free energies (total energies from density functional theory calculations plus the phonon and magnetic free energy contributions) at 200 and 300 K have been added. The free energy curves show that the martensitic transformation in case of Ni_2MnGa occurs between 200 and 300 K in the calculations (see text and Ref. [47] for additional information).

for different Heusler compounds [9,32,33]. All calculations have been performed by using the density functional theory software package VASP (Vienna Ab Initio Simulation Package) employing a plane-wave basis set and the projector augmented wave (PAW) method [34,35]. The exchange correlation part was described in the generalized gradient approximation according to Perdew et al. [36]. The figure shows that two kinds of martensites develop when approaching sufficiently low temperatures, one for $c/a < 1$, the other for $c/a > 1$ where $c/a = 1$ corresponds to the cubic structure. It turns out that the volume change along the tetragonal transformation path is very small. In addition, there exist solutions with monoclinic modulated structures, the so-called M phases. Since their monoclinic angle is small, one may typify them by their tetragonal approximates. All M phases have $c/a < 1$ ratios and emerge from shift of atomic planes in [011] direction. They develop large MAE (magnetic anisotropy energy) which is comparable or larger than the energy needed to form twin boundaries in the modulated structures [37]. The shift of atomic planes may be considered as nucleation centers of twin boundary formation. The large MAE values are

responsible for the magnetic field induced effects and for the MSME of the martensitic phases [38,39].

Figure 2 highlights some finite temperature effects. The arrow in the left panel (“decreasing T ”) illustrates how the low-temperatures $E^M(c/a)$ curves of martensite with two energy minima develop from the $E^A(c/a)$ curves of austenite with a single energy minimum. The right panel contains two ab initio free energy curves of Ni_2MnGa with phonon and magnetic contributions, which show the phase transformation to non-modulated tetragonal $L1_0$ martensite with decreasing temperature [9] (the free energy curves do not contain the transformation to the modulated phases, only the transformation to non-modulated $c/a > 1$ phase has been calculated). The appearance of two energy minima with competing different structures is an exceptional case and is not known to happen in most other martensitic systems. For the magnetic Heusler alloys it can be assigned to the strong influence of magnetism such as the enhanced magnetic susceptibility connected with particular nesting wave vectors of spin-down and spin-up Fermi surfaces on the structural transformation. The sequence of phase transformations,

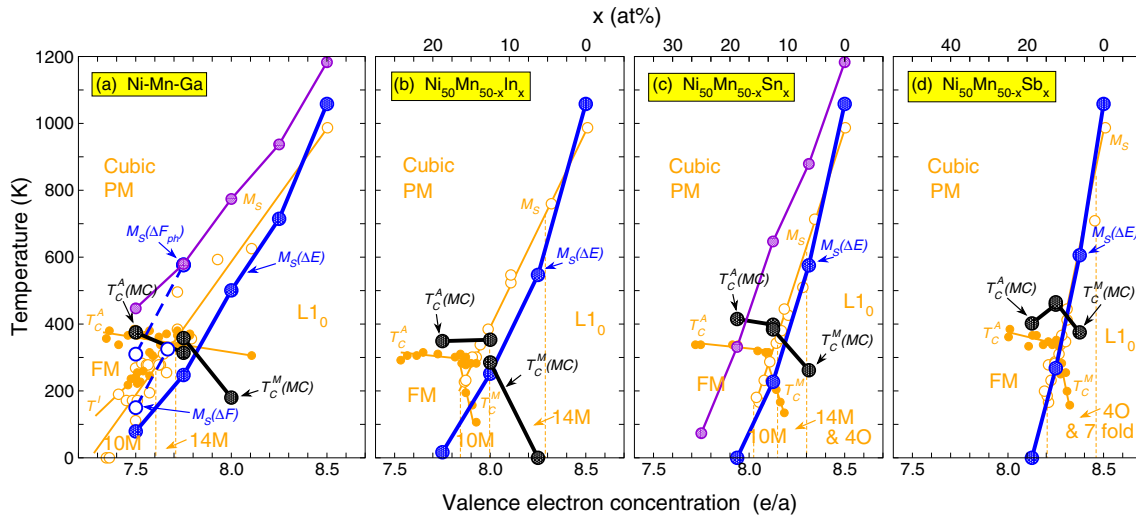


Fig. 3. (Color online) Theoretical phase diagram of $\text{Ni}_2\text{Mn}_{1+x}\text{Z}_{1-x}$ ($\text{Z} = \text{Ga}, \text{In}, \text{Sn}, \text{Sb}$) marked by the blue and black lines and circles compared to the experimental data (orange lines and circles). The blue dots arise from structural energy differences of total energy curves which have been converted to a temperature scale. The violet curves refer to $\text{Ni}_{25}\text{Pt}_{25}\text{Mn}_{50-x}(\text{Ga}, \text{Sn})_x$, respectively. The black curves refer to Monte Carlo calculations of the critical magnetic temperature for austenite and martensite, $T_c^A(\text{MC})$ and $T_c^M(\text{MC})$, respectively. In case of Ni-Mn-Ga, two other methods have been applied to approximate M_S : $M_S(\Delta F_{ph})$ refers to a calculation taking into account the harmonic free energy while $M_S(\Delta F)$ refers to a calculations taking into account also magnetic contributions to the free energy. The data have been taken from various sources [9,10,44–47].

for example, in Ni_2MnGa is from L_{21} austenite to pre-martensite 6M (for the near-stoichiometric samples) and below the martensitic transformation temperature M_S to 10M and 14M and finally to L_{10} at low temperatures [40] (see discussion of modulated phases below).

3 Sequence of martensitic transformations in $\text{Ni}_2\text{Mn}_{1+x}(\text{Ga}, \text{In}, \text{Sn}, \text{Sb})_{1-x}$

All structural transformations in $\text{Ni}_2\text{Mn}_{1+x}(\text{Ga}, \text{In}, \text{Sn}, \text{Sb})_{1-x}$ alloys occur in the (complex) magnetic phase following the sequence from L_{21} austenite to the modulated monoclinic 10M and 14M structures (with periodic shift of layers) to non-modulated tetragonal martensite with decreasing temperature. The periodic shift of layers has been reinterpreted in the frame of nanotwins, which may be convenient when discussing the formation of twin boundaries near the habit plane of austenite and martensite and subsequent coarsening of twin structures away from the habit plane as adaptive martensite (see Refs. [41,42]). On the other hand structural refinements demonstrated that 5M and 7M modulated phases show incommensurate periodicity with respect to the fundamental martensite lattice. The obtained crystal structures are termed 5M (IC) and 7M (IC) where IC stands for incommensurate [23,43].

The martensitic transformation temperature increases strongly with increasing Mn-excess, i.e. increasing number of valence electrons per atom, e/a , until M_S of binary Ni-Mn alloy around 10^3 K is reached. This is shown in Figure 3 where the data have been taken from various sources [9,10,44–47]. The martensitic transformation temperature M_S of the Mn-excess alloys increases linearly

with e/a (see orange data in Fig. 3) and intersects with the magnetic phase transition lines of austenite and martensite for each of the alloy systems. Note that for other compositional trends of the ternary systems such as the Ni-excess samples of $\text{Ni}_{2+x}\text{Mn}_{1-x}\text{Ga}$, the strict linear behavior is less pronounced [3,17].

We would like to emphasize that the experimental sequence of phase transformations of the magnetic Heusler alloys can be reproduced by the theoretical calculations (see, for instance [9–11,47]).

4 Variation of magnetic exchange parameters across the martensitic transformations in $\text{Ni}_2\text{Mn}_{1+x}(\text{Ga}, \text{In}, \text{Sn}, \text{Sb})_{1-x}$

The rather unconventional magnetization curves obtained by experiment show a sharp increase at the Curie temperature of austenite and a sharp drop at lower temperatures when the martensitic transformation to one of the intermediate phases, 10M, 14M, or 4O, is reached (cf. Figs. 3 and 4) [4,5,48,49]. This behavior can be understood when we consider the variation of the magnetic exchange parameters across the different martensitic transformations while passing from the L_{21} structure to the L_{10} one. This is illustrated in Figure 6, which displays the exchange parameters at stoichiometric composition of austenite and at off-stoichiometric composition, $\text{Ni}_2\text{Mn}_{1+x}\text{In}_{1-x}$, with $x = 0.64$, for austenite ($c/a = 1$) and tetragonal martensite ($c/a = 0.94$) (see also Ref. [50]).

The behavior of the experimental magnetization curves (for unsaturated and saturated cases) across the martensitic transformation is associated with the

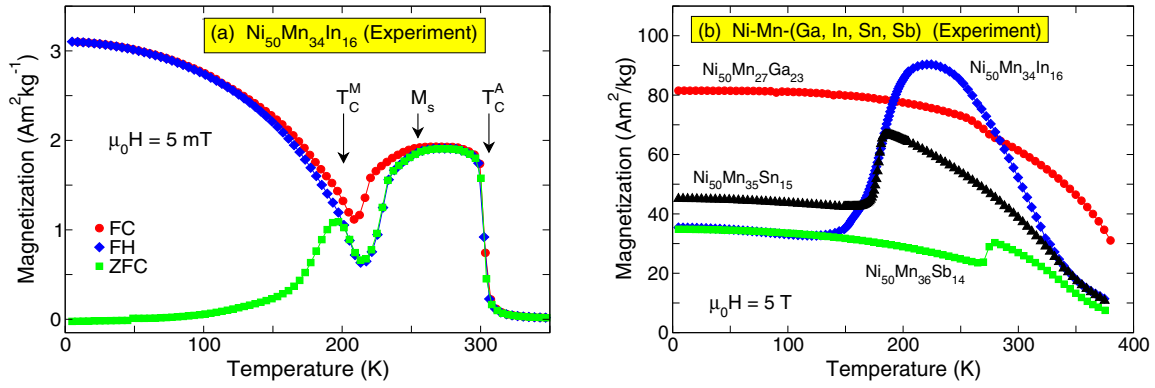


Fig. 4. (Color online) (a) Field cooled (FC), field-heated (FH), and zero-field cooled (ZFC) experimental magnetization curves of $\text{Ni}_{50}\text{Mn}_{34}\text{In}_{16}$ for a small magnetic field $\mu_0 H = 5$ mT. The arrows mark the Curie temperature of the austenitic phase ($T_C^A = 300$ K), the martensitic start temperature ($M_S = 264$ K), and the Curie temperature of the martensitic phase ($T_C^M = 200$ K), respectively. Figure adapted from reference [48]. (b) Saturation magnetization curves of $\text{Ni}_{50}\text{Mn}_{27}\text{Ga}_{23}$, $\text{Ni}_{50}\text{Mn}_{34}\text{In}_{16}$, $\text{Ni}_{50}\text{Mn}_{36}\text{Sn}_{15}$, and $\text{Ni}_{50}\text{Mn}_{36}\text{Sb}_{14}$ at $\mu_0 H = 5$ T.

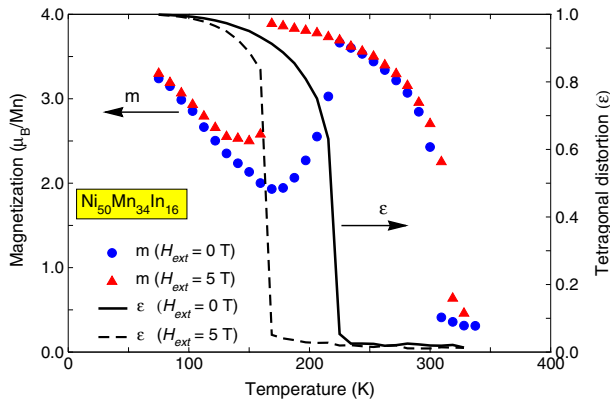


Fig. 5. (Color online) Calculated temperature dependence of magnetization and strain order parameters for $\text{Ni}_{50}\text{Mn}_{34}\text{In}_{16}$ in magnetic fields of 0 and 5 T. Filled circles and triangles refer to magnetization and solid and dashed curves mark the strain order parameter.

appearance of stronger antiferromagnetic exchange parameters below the martensitic transformation, which is connected with disorder, slight change of interatomic distances and reconfiguration of the electronic structure with the onset of martensite. We would like to mention (without going into details) that the temperature variation of the magnetization can be described theoretically by using a model Hamiltonian which contains the magnetic exchange parameters from ab initio calculations [6] and elastic and magnetoelastic interactions terms of which the parameters can be fixed by the experimental martensitic transformations temperature (see Refs. [50–52]). Figure 5 shows resulting magnetization curves and martensitic transformation temperatures of $\text{Ni}_{50}\text{Mn}_{34}\text{In}_{16}$ ($\text{Ni}_2\text{Mn}_{1.36}\text{In}_{0.64}$) for different external magnetic fields. The magnetization curve for a field of 5 T agrees well with the corresponding experimental curve in Figure 4b. Also the experimental shift of the structural transformation to lower temperatures in a field of 5 T is reproduced.

5 Impact of magnetism on phase diagrams, Fermi surface nesting and monoclinic structures

5.1 Impact of magnetism on phase diagrams

The change of magnetic exchange parameters across the structural phase transformations discussed above reveals the strong influence of environmental changes on the electronic structure and magnetic configurations. For instance, if we use the valence electron number per atom (e/a) as in Figure 3 in order to characterize the phase diagrams, we observe the linear increase of the martensitic start temperature M_S with increasing e/a . This can be explained by using a modified Slater-Pauling plot as in Figure 7 which shows the number of reversed Mn spins over the whole e/a range for each of the Mn-excess alloys, $\text{Ni}_2\text{Mn}_{1+x}\text{Z}_{1-x}$ with $Z = \text{Ga, In, Sn or Sb}$. Although, we cannot discuss all electronic structure changes with e/a in detail here, it is obvious that from supercell calculations for 16-atoms $\text{Ni}_8\text{Mn}_{4+x}\text{Z}_{4-x}$ cells that, since the Mn-moment is rather localized and reverses its spin when being placed on a Z-lattice site, the number of Mn atoms with spin-down increases in a linear way with e/a , i.e. with the number of increasing Mn-excess atoms. This explains the linear increase of M_S with increasing e/a .

5.2 Impact of magnetism on the Fermi surface topology

Strong Fermi surface nesting (Fig. 8) has been observed at stoichiometric composition of Ni_2MnGa which has been taken as a hint that the observed Kohn-like anomalies associated with the Fermi surface nesting wave vector $\mathbf{q} = (\frac{1}{3}\frac{1}{3}0)(2\pi/a)$ is responsible for phonon softening in austenite and the premartensitic transformation [47,53–57]. Indeed, the generalized susceptibility

$$\chi_{\sigma}^0(\mathbf{q}, \omega) = \sum_{\mathbf{k}n n'} \frac{f_{\mathbf{k}n\sigma} - f_{\mathbf{k}+\mathbf{q}n'\sigma}}{\varepsilon_{\mathbf{k}n\sigma} - \varepsilon_{\mathbf{k}+\mathbf{q}n'\sigma} - \hbar\omega - i0^+}, \quad (1)$$

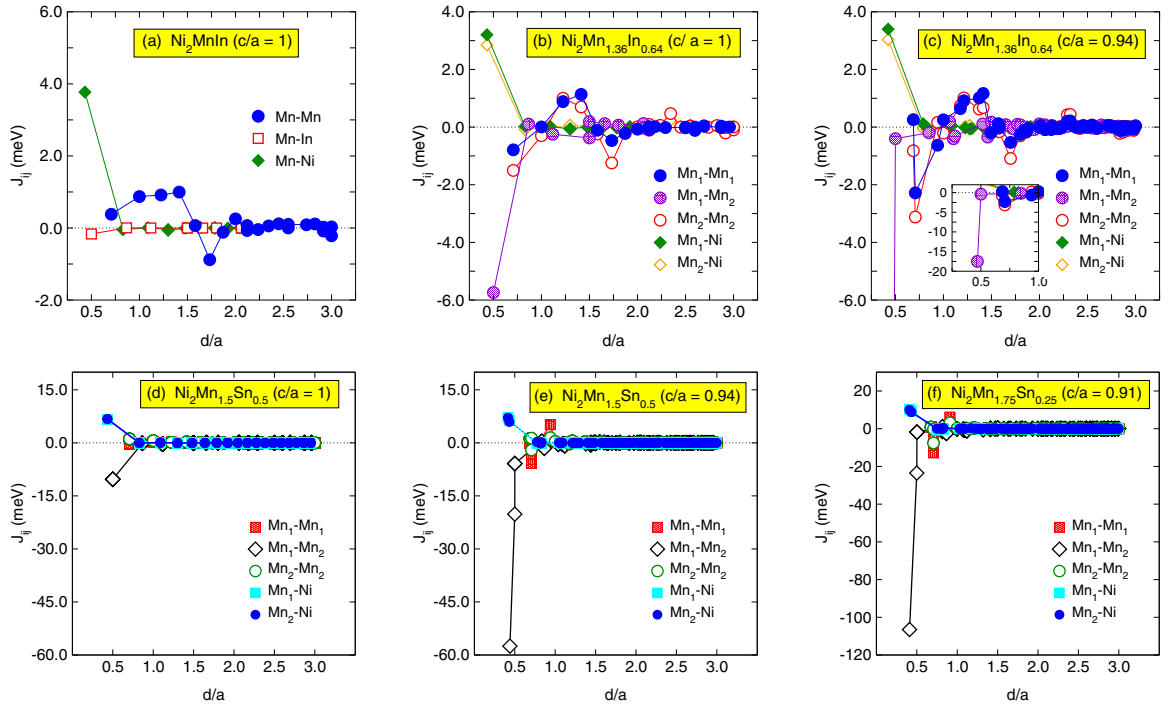


Fig. 6. (Color online) Calculated magnetic exchange parameters of $\text{Ni}_2\text{Mn}_{1.36}\text{In}_{0.64}$ ($\text{Ni}_{50}\text{Mn}_{34}\text{In}_{16}$) as a function of the distance between the atoms in units of the lattice constant a [50]. Positive J_{ij} denote ferromagnetic interactions, negative ones denote antiferromagnetic interactions. For comparison (a) highlights the results for the stoichiometric compound in the cubic phase while (b) shows the results for the off-stoichiometric composition in the cubic phase and (c) for the off-stoichiometric composition and a tetragonal distortion of $c/a = 0.94$. The increase of the strength of antiferromagnetic interactions from (a) to (c) can be clearly noticed. (d)–(f) are the results for off-stoichiometric Ni-Mn-Sn alloys.

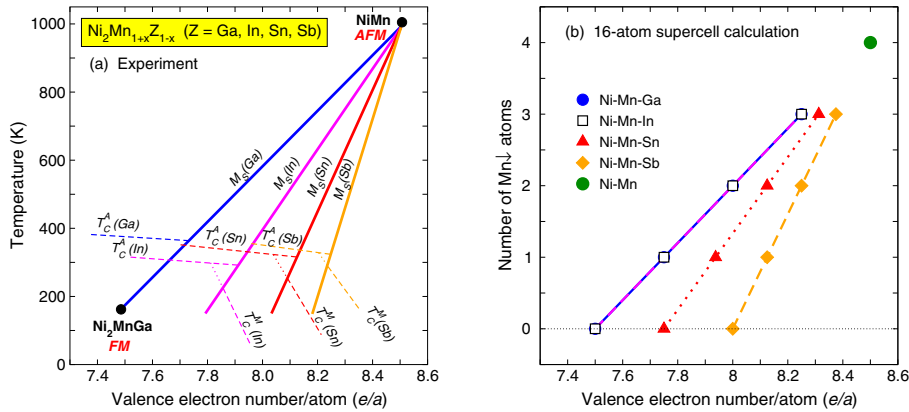


Fig. 7. (Color online) (a) Experimental phase diagram of $\text{Ni}_2\text{Mn}_{1+x}\text{Z}_{1-x}$ showing the different slopes of the martensite transformation temperature M_S for each alloy system. Figure adapted from reference [4]. (b) Number of antiferromagnetically aligned Mn atoms in a supercell of 16 atoms as a function of e/a for the same alloys. The data for Ni-Mn-Ga and Ni-Mn-In lie on top of each other. The binary system NiMn is an antiferromagnet with vanishing total magnetization.

where $f_{\mathbf{k}n\sigma}$ is the Fermi distribution function, ω is the frequency and $\varepsilon_{\mathbf{k}n\sigma}$ the quasiparticle energy with momentum \mathbf{k} , band index n and spin σ , exhibits peaks for both majority and minority bands of Ni_2MnGa in the austenitic phase. Since the susceptibility enters the electron-phonon coupling matrix elements, second order perturbation theory leads to a renormalized phonon spectrum and softening of the transverse acoustic branch as observed in

neutron scattering experiments for Ni_2MnGa alloys with near-stoichiometric composition [58–62].

The experimentally determined Fermi surface sheets from two-dimensional angular correlation of electron-positron annihilation radiation [57] support the nesting features observed in the ab initio calculation. Namely, the softening in austenite and in 6M (or 3M) premartensite of Ni_2MnGa for $M_S < T < 260$ K. The symmetry

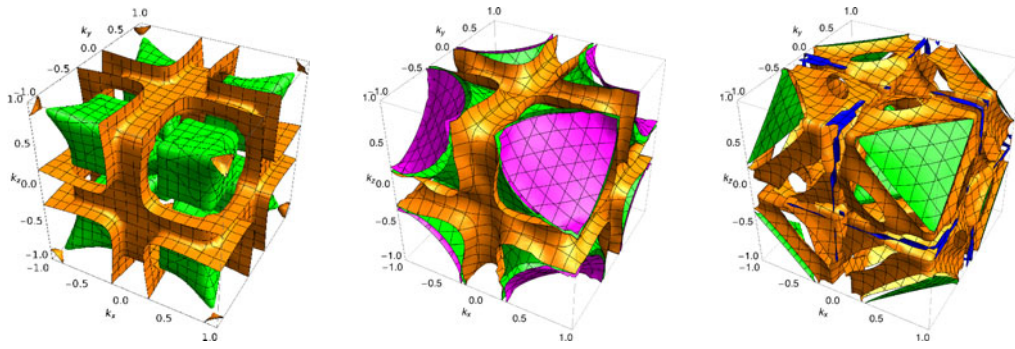


Fig. 8. (Color online) Calculated spin-down (left) and spin-up (middle) Fermi surfaces of Ni_2MnGa . The minority Fermi surface shows the 13th (green) hole sheet and the 14th (orange) minority electron sheet. Strong nesting is found for the 14th minority electron sheet with wave vector $\mathbf{q} = (\frac{1}{3}\frac{1}{3}0)(2\pi/a)$. The 17th majority hole sheet shows nesting behavior in $[110]$ direction as well [53] although the charge-charge susceptibility is less compared to one of minority-spin carriers. Electron-positron annihilation experiments confirm the nesting features of Ni_2MnGa [57]. The right panel shows the Fermi surface of the antiferromagnet NiMn which still exhibits nesting features that have survived when going from pseudobinary Ni_2MnGa to binary NiMn .

of the premartensitic phase is still cubic but the atoms assume modulated positions with nearly six-plane period along $[110]$ direction and a phonon anomaly in the TA_2 branch. Ab initio calculations of phonon dispersions have confirmed the experimental findings, for example (see Refs. [55,63–66]). While Fermi surface nesting and enhanced charge susceptibility (Kohn anomaly) will play a role in the structural phase transformation it has been argued that the formation of martensite may also be driven by the band Jahn-Teller effect whereby the $3d-e_g$ minority band is driven towards the Fermi energy assuming that the Jahn-Teller splitting has an impact on the structural instability of the cubic phase [67,68]. More recent investigations of the competition of ferromagnetic and antiferromagnetic interactions allow to conclude that the accompanying magnetic softness of the lattice and the strengthening of the antiferromagnetic contribution with increasing atomic disorder may enforce the instability of the cubic structure leading to a variety of modulated orthorhombic and monoclinic martensitic phases.

We have performed additional calculations of the evolution of Fermi surfaces of $\text{Ni}_2\text{Mn}_{1+x}(\text{Ga}, \text{Sn})_{1-x}$ for extra Mn on the Ga and Sn sites ($x = 0.1, 0.2, 0.3, 0.4$ and 0.5) and observe that nesting behavior of the stoichiometric compositions prevails in the alloys with extra Mn [69]. So, we may tentatively conclude that the crossover from ferromagnetism in ternary $\text{Ni}_2\text{Mn}(\text{Ga}, \text{Sn})$ compounds to antiferromagnetism of binary NiMn alloys does not destroy the nesting behavior of the austenitic phases (see Fig. 8). This is because most electronic states at the Fermi surface arise from the Ni states at the upper edge of the pseudogap (remaining of the semiconducting gap of the full Heusler alloys) which have e_g symmetry and which do not hybridize strongly with the Mn states. Therefore, the charge susceptibility (especially in the spin-down channel) and Kohn anomaly are still enhanced in the alloy cases. The extra valence electrons of Mn just increase the volume of the Fermi surface.

Combined theoretical and experimental investigations show that the main change related to the reconfiguration

of the Fermi surface while passing from austenite to premartensite ($T_{PM} \sim 247$ K) and to martensite ($T_M \sim 196$ K), is associated with the shift of the $\text{Ni}-e_g$ peak from below the Fermi energy to an energy above E_F [9,70].

5.3 Impact of magnetism on the monoclinic structures

The 6M (3M) modulation of the premartensitic phase of Ni_2MnGa changes to monoclinic 10M (5M) respective 14M (7M) when the system enters the martensitic state below 200–220 K. We may also expect modulated 4O or 6O martensite for Mn deficiency or when replacing Ga by Sn or Sb. Note that premartensite of Ni_2MnGa vanishes in Mn-rich samples or shrinks to a small portion when compressive stress is applied. If we neglect the monoclinicity and calculate tetragonal martensite with $c/a = 0.94$, then the nesting vector of Ni_2MnGa changes from 0.33 in austenite to 0.43 in martensite [55]. Measurements of phonon dispersions of martensite confirm this nesting behavior [71,72], as well as measurements from which the Fermi surface could be extracted [57]. The neutron scattering experiments became possible because of the stabilization of the martensitic phase by an external magnetic field [71,72].

A new feature appears for the 0.43 nesting case reminiscent to the instability of a one-dimensional metal (Peierls instability), which is accompanied by the formation of an energy gap and a charge-density wave arising from parallel Fermi surface sheets with nesting vector $2k_F$ being usually incommensurate. Indeed, the origin of this 0.43 satellite peak can be related to modulation of atomic ($0k0$) planes (as an example see Fig. 1b). The analysis of powder X-ray diffraction based on an orthorhombic structure yields an incommensurately modulated four-dimensional base [73],

$$\mathbf{H} = h\mathbf{a}^* + k\mathbf{b}^* + l\mathbf{c}^* + \mathbf{q}, \quad \mathbf{q} = 0.43\mathbf{b}^*. \quad (2)$$

Shapiro et al. [72] explained the corresponding phonon anomaly as the phason mode associated with the

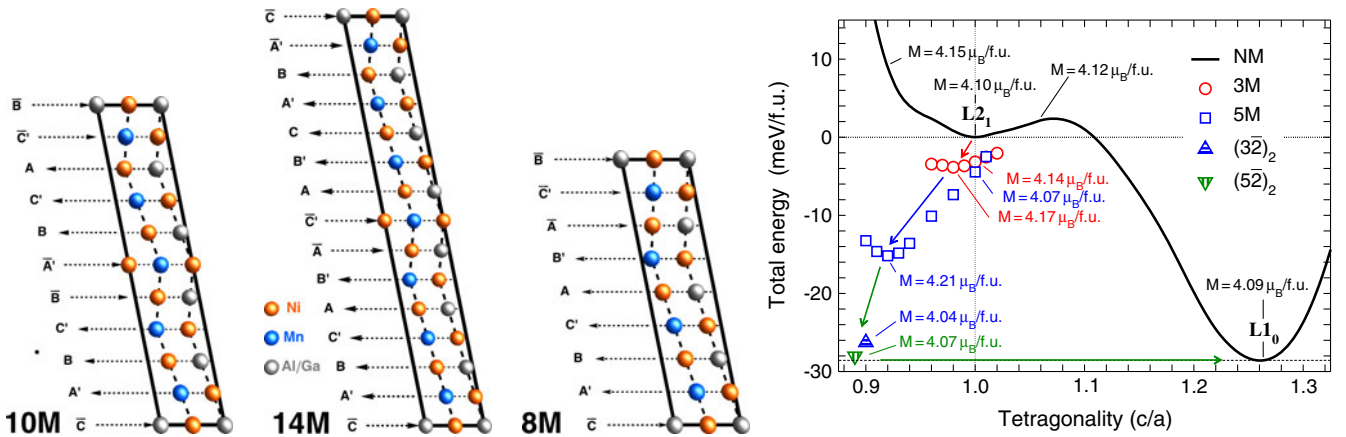


Fig. 9. (Color online) Left: monoclinic structures 10M, 14M and 8M. Right: total energies (per formula unit) of non-modulated (NM) and modulated monoclinic structures (3M, 5M, 10M-($3\bar{2}$)₂ and 14M-($5\bar{2}$)₂) of Ni₂MnGa relative to the L₂₁ ($c/a = 1$) structure obtained from high-precision ab initio calculations. Since the modulated structures are slightly monoclinic, the corresponding c/a values are approximate. The ground state is the NM structure with $c/a = 1.26$ (L₁₀) while 10M and 14M structures have slightly higher energies (the latter by 0.38 meV).

quasi-one-dimensional charge density wave, although, the amplitude mode was not found in the measurements. Note that recently a charge density wave associated with an incommensurate periodic lattice distortion on the Ni₂MnGa surface in the ferromagnetic phase has been observed [74].

The intermediate martensite structures are even more rich if we consider Ni₂MnAl where Al is isoelectronic to Ga. Aging effects were observed for the B2/L₂₁ ordering temperatures depending on disorder in the Ni-Al-Mn system. The martensitic product phases found are the 2M phase with stacking sequence (1)₂, the 10M with stacking sequence ($5\bar{2}3\bar{2}$), the 12M phase with stacking sequence ($5\bar{2}$)₂ and the 14M phase with stacking sequence ($5\bar{2}$)₂ and the 8M phase with a stacking periodicity eight times that of the (220)_{L₂₁} lattice planes or ($5\bar{3}$). The 10M product phase appears for near stoichiometric compositions. For details and earlier references, see reference [75].

For Ni-Mn-Ga alloys, the premartensitic and intermartensitic phases are the 6M (3M), the 10M (5M) respective ($3\bar{2}$)₂ and the 14M (7M) respective ($5\bar{2}$)₂. It should be noted that the “5M” and “7M” structures are preferentially incommensurate.

Figure 9 shows the typical modulation of atoms of the 10M, 14M and 8M structures [3,75]. The 10M and 14M structures are realized both in the pseudobinary alloy series Ni-Mn-(Al, Ga, In, Sn, Sb). The interesting aspect is that strong ferromagnetism exists in Ni-Mn-(Ga, In, Sn, Sb) with a crossover to antiferromagnetism with increasing c/a and increasing atomic disorder. Hence, it is interesting to check how far magnetism determines the stability of the structures, too. Figure 9 also shows the energetic sequence of modulated structures of Ni₂MnGa close to L₂₁ which were obtained from ab initio calculations at zero temperature (see also Ref. [76]). Mn is mainly determining the magnetic moment, which is about 4 μ_B on the average for austenite and resulting modulated martensite structures (see Fig. 9). But the average moment quickly decreases with increasing concentration of antiferromagnetic Mn-clusters in the ferromagnetic matrix.

In order to obtain the accurate results presented in Figure 9, we used the VASP code [34,35] and considered a large basis with a plane wave cut-off of 460 eV, explicitly taking into account the $3d^{10}4s^1$ electrons for Ga, $3p^63d^94s^1$ for Ni and $3p^63d^64s^1$ for Mn. The exchange correlation part was described in the generalized gradient approximation according to Perdew et al. [36]. Convergence of the electronic structure was assumed, when changes between two consecutive steps fell below 10^{-7} eV, geometric optimizations were performed until the largest residual forces were in the order of 0.002 eV/Å.

The nonmodulated structure (NM) was described within the 4-atom primitive cell, while for the modulated structures 8-atom building blocks were employed with a and b axes rotated by 45° with respect to the conventional unit cell. These were stacked 3×, 5×, and 7× along the b axis ([110] crystal direction) in order to allow for respective modulations. In addition to the geometric optimizations of the atomic positions, we also varied the cell shape. For the conventional 3M and 5M modulations we assumed pseudo-tetragonal structures by restricting to tetragonal deformations of the 8-atom building blocks of the supercells. In a separate calculation we allowed for a full monoclinic variation of the supercell.

For cubic lattice parameters corresponding to the L₂₁ structure, we find in accordance with the soft acoustic phonon in [110] direction that modulations lower the energy in the order of 4 meV/f.u. The energy gain is slightly higher for the 5-fold than for the 3-fold modulation in agreement with previous results [77]. The lower symmetry induced by both kinds of modulation induces, however, stresses on the simulation cell which are not present in the L₂₁ case. In consequence, the modulated structures gain energy with tetragonal lattice parameters. Minimum energy is achieved at $c/a = 0.985$ for the 3M and at $c/a = 0.92$ for the 5M, respectively.

While the pseudo-tetragonal 3M cell is practically stress free and remains nearly tetragonal even after extensive constraint-free optimizations, the pseudo-tetragonal

5M structure is subject to residual stresses which induce further relaxations leading to a monoclinic cell shape, with a and b axes slightly different in length and non-rectangular with respect to each other. The corresponding result is shown in Figure 9 by the upward triangle. The internal structure resembles of a $(3\bar{2})_2$ sequence where the shear direction of the block of layers is smoothly changed. This structural detail diverges from the classical nanotwinned adaptive model where the different blocks with opposite directions are related by a flat mirror plane. The smoothed pathways of atomic layers is similar to the modulated crystallographic structure obtained by structural refinement in references [23,43].

The corresponding energy is considerably lower than that of the pseudo-tetragonal structure and close to the absolute minimum of the energy corresponding to the non-modulated tetragonal $L1_0$ martensite. Still the energy can be lowered by stacking five and two $L1_0$ non-modulated martensites into the simulation cell, which is represented by the green downward triangle in Figure 9. This $(5\bar{2})_2$ adaptive martensite corresponds to the 14M structure frequently found in experiment, too. For a discussion of adaptive features and twin formation when a twin plate is of a certain width has nucleated in the austenitic structure, we refer to [41,42].

From the energetic pattern displayed in Figure 9, one is led to the following scenario for the appearance of the modulated structures: starting from the cubic $L2_1$ phase above the martensite start temperature M_S , soft phonons (and competing magnetic interactions) induce a modulation of the structure, which can be (eventually depending on the magnetization) either of 3-fold or directly of 5-fold type. These modulations directly induce a change of the cell parameters. While a pseudo-tetragonal structure which easily adapts to the austenite, is stable for the 3M phase initially, it may change its modulation to 5M, as this modulation can gain more energy on further decrease of c/a . Still, pseudo-tetragonality may be enforced from the austenite-martensite interface. If this is not the case, a fully monoclinic nanotwinned structure will appear, which again is considerably lower in energy. Finally, the plane shifting can rearrange in order to form the 14M adaptive structure observed in many experiments.

Besides for the modulated monoclinic structures, one encounters such plane shifting also in the usual bcc-hcp transformation [29,30] highlighted in Figure 1d, which can lower the elastic energy and can cause considerable softening of the lattice. We show in Figure 10 the result of the bcc-hcp transformation for Ni_2MnGa and Pt_2MnGa along the Burgers path transformation. Note that for other magnetic Heusler alloys like Co_2NiGa and other Co-based systems the bcc-hcp transformation may occur spontaneously since there is no energy barrier [78]. $\text{Ni}_{1-x}\text{Pt}_x\text{MnGa}$ is an interesting magnetic shape memory-system which exhibits a 7M orthorhombic modulated structure together with a charge density wave as inferred from neutron scattering experiment [79].

Finally, we would like to emphasize that the different M structures and their corresponding tetragonal counter

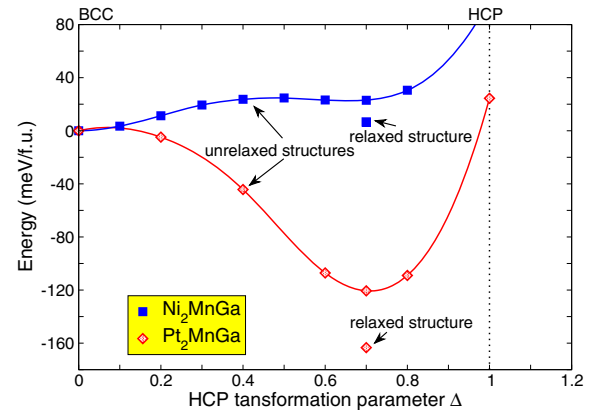


Fig. 10. (Color online) Ab initio results for the bcc-hcp transformation along the Burgers path for Ni_2MnGa and Pt_2MnGa . For Pt_2MnGa the minimum along the transformation path is close to the energy of the 14M structure which is slightly above the ground state with tetragonality $c/a = 1.31$.

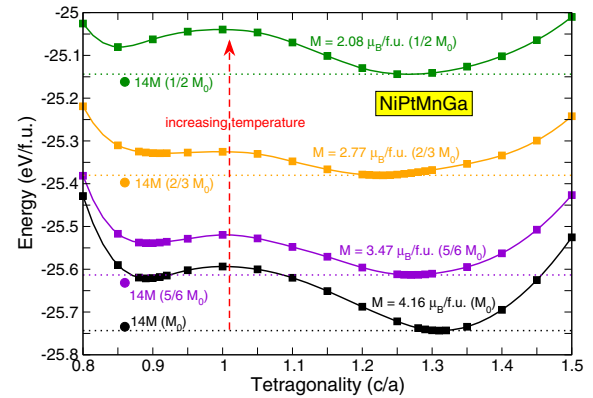


Fig. 11. (Color online) Ab initio results for 14M and corresponding $c/a > 1$ structures calculated for different fixed magnetization values using the fixed spin moment method. Decreasing fixed spin moment values are a measure of increasing temperature. We observe that the energy of the tetragonal minimum structure increases faster with temperature than the 14M solution. Or, upon lowering the temperature of austenite, the 14M structure with $c/a < 1$ develops a minimum before the $c/a > 1$ manifests itself on the energy landscape.

parts are independent solutions in spite of the similarity of 14M and $c/a > 1$ structures. In order to demonstrate this, we show in Figure 11 the different temperature evolution of both structures for the case of NiPtMnGa .

6 Conclusions

First-principles calculations of the phase diagrams of the functional Heusler alloy series $\text{Ni}_2\text{Mn}_{1+x}(\text{Ga}, \text{In}, \text{Sn}, \text{Sb})_{1-x}$ confirm the experimental observation of competing magnetic interactions. The martensitic transformation temperature $M_S(e/a)$ is proportional to the concentration of antiferromagnetically aligned spin moments of Mn which increases with e/a (or, in other words, M_S approximately scales with the nearest neighbor antiferromagnetic Mn-Mn exchange interaction parameter: $M_S \propto J_{ij}^{AFM}$). The strong decrease of the magnetization

below the martensitic transformation temperature as observed experimentally can be explained by the change of the magnetic exchange parameters across M_S . Details of the modulated structures have been discussed.

The resulting complex magnetic configurations are to a large extent responsible for most of the related multifunctional properties of the martensitic phases such as the magnetic shape-memory, exchange bias and magnetocaloric effects. Other interesting properties still need to be investigated but will require large-scale computations and model building, for instance, the formation of spin-cluster glasses and calculation of the exchange bias effect and strain-glass effects in the precursor phases of martensite.

P.E. and M.E.G. acknowledge financial support by the Deutsche Forschungsgemeinschaft within the Priority Programme SPP 1239.

References

1. *Magnetism and Structure in Functional Materials*, edited by A. Planes, L. Mañosa, A. Saxena (Springer, Berlin, 2005), Vol. 79
2. *Half-metallic Heusler alloys – Fundamentals and Applications*, edited by I. Galanakis, P.H. Dederichs (Springer, Berlin, 2005), Vol. 676
3. P. Entel, V.D. Buchelnikov, V.V. Khovailo, A.T. Zayak, W.A. Adeagbo, M.E. Gruner, H.C. Herper, E.F. Wassermann, J. Phys. D **39**, 865 (2006)
4. A. Planes, L. Mañosa, M. Acet, J. Phys.: Condens. Matter **21**, 233201 (2009)
5. M. Acet, L. Mañosa, A. Planes, in *Handbook of Magnetic Materials*, edited by K.H.J. Buschow (Elsevier, Amsterdam, 2011), Vol. 19, p. 231
6. P. Entel, A. Dannenberg, M. Siewert, H.C. Herper, M.E. Gruner, V.D. Buchelnikov, V.A. Chernenko, Mater. Sci. Forum **684**, 1 (2011)
7. T. Graf, C. Felser, S.S.P. Parkin, Prog. Solid State Chem. **39**, 1 (2011)
8. P. Entel, M.E. Gruner, A. Hucht, A. Dannenberg, M. Siewert, H.C. Herper, T. Kakeshita, T. Fukuda, V.V. Sokolovskiy, V.D. Buchelnikov, in *Disorder and Strain-Induced Complexity in Functional Materials*, edited by T. Kakeshita, T. Fukuda, T. Saxena, A. Planes (Springer, Berlin, 2012), Vol. 148, p. 19
9. P. Entel, A. Dannenberg, M. Siewert, H.C. Herper, M.E. Gruner, D. Comtesse, H.-J. Elmers, M. Kallmayer, Metal. Mater. Trans. A **43**, 2891 (2012)
10. P. Entel, M. Siewert, M.E. Gruner, A. Chakrabarti, S.R. Barman, V.V. Sokolovskiy, V.D. Buchelnikov, J. Alloys Compd. (2012), DOI:10.1016/j.jallcom.2012.03.005, in press
11. M. Siewert, M.E. Gruner, A. Hucht, H.C. Herper, A. Dannenberg, A. Chakrabarti, N. Singh, R. Arroyave, P. Entel, Adv. Eng. Mater. **14**, 530 (2012)
12. A.K. Pathak, M. Khan, B.R. Gautam, S. Stadler, I. Dubenko, N. Ali, J. Magn. Mater. **321**, 963 (2009)
13. H.C. Xuan, Q.Q. Cao, C.L. Zhang, S.C. Ma, S.Y. Chen, D.H. Wang, Y.W. Du, Appl. Phys. Lett. **96**, 202502 (2010)
14. K.P. Bhatti, S. El-Khatib, V. Srivastava, R.D. James, C. Leighton, Phys. Rev. B **85**, 134450 (2012)
15. R.C. O'Handley, J. Appl. Phys. **83**, 3263 (1998)
16. F. Albertini, F. Canepa, S. Cirafici, E.A. Franceschi, M. Napolitano, A. Paoluzi, L. Pareti, M. Solzi, J. Magn. Mater. **272-276**, 2111 (2004)
17. V.V. Khovailo, V. Novosad, T. Takagi, D.A. Filippov, R.Z. Levitin, A.N. Vasilev, Phys. Rev. B **70**, 174413 (2004)
18. C.V. Stager, C.M. Campbell, Can. J. Phys. **56**, 674 (1978)
19. K. Ullakko, J.K. Huang, C. Kantner, R.C. O'Handley, V.V. Kokorin, Appl. Phys. Lett. **69**, 1966 (1996)
20. A. Sozinov, A.A. Likhachev, N. Lanska, K. Ullakko, Appl. Phys. Lett. **80**, 1746 (2002)
21. H. Morito, K. Oikawa, A. Fujita, K. Fukumichi, R. Kainuma, K. Ishida, J. Phys.: Condens. Matter **21**, 256002 (2009)
22. M. Siewert, M.E. Gruner, A. Dannenberg, A. Chakrabarti, H.C. Herper, M. Wuttig, S.R. Barman, S. Singh, A. Al-Zubi, T. Hickel, J. Neugebauer, M. Gillessen, R. Dronskowski, P. Entel, Appl. Phys. Lett. **99**, 191904 (2011)
23. L. Righi, F. Albertini, L. Pareti, A. Paoluzi, G. Calestani, Acta Mater. **55**, 5237 (2007)
24. F.A. Hames, J. Crangle, J. Appl. Phys. **42**, 1336 (1971)
25. Y. Kishi, Z. Yajima, K. Shimizu, M. Wuttig, Mater. Sci. Eng. A **378**, 361 (2004)
26. M. Gillessen, R. Dronskowski, J. Comput. Chem. **31**, 612 (2009)
27. E.C. Bain, Trans. Am. Inst. Min. Metall. Pet. Eng. **70**, 25 (1924)
28. C. Engin, L. Sandoval, H. Urbassek, Model. Simul. Mater. Sci. Eng. **16**, 035005 (2008)
29. W.G. Burgers, Physica **1**, 561 (1934)
30. S.R. Nishitani, H. Kawabe, M. Aoki, Mater. Sci. Eng. A **312**, 77 (2001)
31. E. Uhl, J. Solid State Chem. **43**, 354 (1982)
32. A. Dannenberg, M.E. Gruner, M. Wuttig, P. Entel, Mater. Res. Soc. Symp. Proc. **1200E**, 1200-G04-03 (2010)
33. A. Dannenberg, M. Siewert, M.E. Gruner, M. Wuttig, P. Entel, Phys. Rev. B **82**, 214421 (2010)
34. G. Kresse, J. Furthmüller, Phys. Rev. B **54**, 11169 (1996)
35. G. Kresse, D. Joubert, Phys. Rev. B **59**, 1758 (1999)
36. J.P. Perdew, K. Burke, M. Ernzerhof, Phys. Rev. Lett. **77**, 3865 (1996)
37. F. Albertini, L. Morellon, P.A. Algarabel, M.R. Ibarra, L. Pareti, Z. Arnold, G. Calestani, J. Appl. Phys. **89**, 5614 (2001)
38. A. Sozinov, A.A. Likhachev, K. Ullakko, IEEE Trans. Magn. **38**, 13422 (2002)
39. V. L'vov, V. Chernenko, Mater. Sci. Forum **684**, 31 (2011)
40. V.A. Chernenko, C. Seguí, E. Cesari, J. Pons, V.V. Kokorin, Phys. Rev. B **57**, 2659 (1998)
41. S. Kaufmann, U.K. Rößler, O. Heczko, M. Wuttig, J. Buschbeck, L. Schultz, S. Fähler, Phys. Rev. Lett. **104**, 145702 (2010)
42. A.G. Khachatryan, S.M. Shapiro, S. Semenovskaya, Phys. Rev. B **43**, 10832 (1991)
43. L. Righi, F. Albertini, E. Villa, A. Paoluzi, G. Calestani, V. Chernenko, S. Besseghini, C. Ritter, F. Passaretti, Acta Mater. **56**, 4529 (2008)
44. V.A. Chernenko, E. Cesari, V.V. Kokorin, I.N. Vitenko, Scripta Metall. Mater. **33**, 1239 (1995)
45. V.A. Chernenko, Scripta Mater. **40**, 523 (1999)

46. S. Aksoy, M. Acet, E.F. Wassermann, T. Krenke, X. Moya, L. Mañosa, A. Planes, P. Deen, *Phil. Mag.* **89**, 2093 (2009)
47. M.A. Uijttewaal, T. Hickel, J. Neugebauer, M.E. Gruner, P. Entel, *Phys. Rev. Lett.* **102**, 035702 (2009)
48. T. Krenke, M. Acet, E.F. Wassermann, X. Moya, L. Mañosa, A. Planes, *Phys. Rev. B* **73**, 174413 (2006)
49. X. Moya, L. Mañosa, A. Planes, S. Aksoy, M. Acet, E.F. Wassermann, T. Krenke, *Phys. Rev. B* **75**, 184412 (2007)
50. V.D. Buchelnikov, P. Entel, S.V. Taskaev, V.V. Sokolovskiy, A. Hucht, M. Ogura, H. Akai, M.E. Gruner, S.K. Nayak, *Phys. Rev. B* **78**, 184427 (2008)
51. V.D. Buchelnikov, V.V. Sokolovskiy, H.C. Herper, H. Ebert, M.E. Gruner, S.V. Taskaev, V.V. Khovaylo, A. Hucht, A. Dannenberg, M. Ogura, H. Akai, M. Acet, P. Entel, *Phys. Rev. B* **81**, 094411 (2010)
52. V.D. Buchelnikov, V.V. Sokolovskiy, S.V. Taskaev, V.V. Khovaylo, A.A. Aliev, L.N. Khanov, A.B. Batdalov, P. Entel, H. Miki, T. Takagi, *J. Phys. D* **44**, 064012 (2011)
53. Y. Lee, J.Y. Rhee, B.N. Harmon, *Phys. Rev. B* **66**, 054424 (2002)
54. O.I. Velikokhatnyĭ, I.I. Naumov, *Phys. Solid State* **41**, 617 (2002)
55. C. Bungaro, K.M. Rabe, A. Dal Corso, *Phys. Rev. B* **68**, 134104 (2003)
56. P. Entel, V.D. Buchelnikov, M.E. Gruner, A. Hucht, V.V. Khovailo, S.K. Nayak, A.T. Zayak, *Mater. Sci. Forum* **583**, 21 (2008)
57. T.D. Haynes, R.J. Watts, J. Laverock, Zs. Major, M.A. Alam, J.W. Taylor, J.A. Duffy, S.B. Dugdale, *New J. Phys.* **14**, 035020 (2012)
58. A. Zheludev, S.M. Shapiro, P. Wochner, A. Schwartz, M. Wall, L.E. Tanner, *J. Phys. IV* **54**, 1139 (1995)
59. A. Zheludev, S.M. Shapiro, P. Wochner, L.E. Tanner, *Phys. Rev. B* **54**, 15045 (1996)
60. U. Stuhr, P. Vorderwisch, V.V. Kokorin, P.-A. Lindgard, *Phys. Rev. B* **56**, 14360 (1997)
61. U. Stuhr, P. Vorderwisch, V.V. Kokorin, *J. Phys.: Condens. Matter* **12**, 7541 (2000)
62. L. Mañosa, A. Planes, J. Zarestky, T. Lograsso, D.L. Schlagel, C. Stassis, *Phys. Rev. B* **64**, 024305 (2001)
63. A.T. Zayak, P. Entel, J. Enkovaara, A. Ayuela, R.M. Nieminen, *Phys. Rev. B* **68**, 134104 (2003)
64. A.T. Zayak, P. Entel, J. Magn. Magn. Mater. **290-291**, 874 (2005)
65. A.T. Zayak, P. Entel, K.M. Rabe, W.A. Adeagbo, M. Acet, *Phys. Rev. B* **72**, 054113 (2005)
66. M. Siewert, M.E. Gruner, A. Dannenberg, A. Hucht, S.M. Shapiro, G. Xu, D.L. Schlagel, T.A. Lograsso, P. Entel, *Phys. Rev. B* **82**, 064420 (2010)
67. S. Fujii, S. Ishida, S. Asano, *J. Phys. Soc. Jpn* **58**, 3657 (1989)
68. A. Ayuela, J. Enkovaara, K. Ullakko, R.M. Nieminen, *J. Phys.: Condens. Matter* **11**, 2017 (1999)
69. M. Alberto, A. Ernst, P. Entel, unpublished data, 2012
70. C.P. Opeil, B. Mihaila, R.K. Schulze, L. Mañosa, A. Planes, W.L. Hults, R.A. Fisher, P.S. Riseborough, P.B. Littlewood, J.L. Smith, J.C. Lashley, *Phys. Rev. Lett.* **100**, 165703 (2008)
71. P. Vorderwisch, S.M. Shapiro, *Mater. Sci. Eng. A* **438-440**, 450 (2006)
72. S.M. Shapiro, P. Vorderwisch, K. Habicht, K. Hradil, H. Schneider, *Europhys. Lett.* **77**, 56994 (2007)
73. L. Righi, F. Albertini, G. Calestani, L. Paretti, A. Paoluzi, C. Ritter, P.A. Algarabel, L. Morellon, R. Ibarra, *J. Solid State Chem.* **179**, 3525 (2006)
74. S.W. D'Souza, A. Rai, J. Nayak, M. Maniraj, R.S. Dhaka, S.R. Barman, D.L. Schlagel, T.A. Lograsso, A. Chakrabarti, *Phys. Rev. B* **85**, 085123 (2012)
75. R. Kainuma, F. Gejima, Y. Sutou, I. Ohnuma, K. Ishida, *Mater. Trans. Jpn Int. Met.* **41**, 943 (2000)
76. R. Niemann, U.K. Röbler, M.E. Gruner, O. Heczko, L. Schultz, S. Fähler, *Adv. Eng. Mater.* **14**, 562 (2012)
77. T. Hickel, M. Uijttewaal, B. Grabowski, J. Neugebauer, *Mater. Res. Soc. Symp. Proc.* <http://dx.doi.org/10.1557/PROC-1050-BB03-02> (2008)
78. A. Talapatra, R. Arroyave, P. Entel, unpublished simulation results, 2012
79. S. Singh, K.R.A. Ziebeck, E. Suard, P. Rajput, S. Bhardwaj, A.M. Awasthi, S.R. Barman, *Appl. Phys. Lett.* **101**, 171904 (2012)